

# Dispersion Analysis of Periodic Structures in Anisotropic Media: Application to Liquid Crystals

Antonio Alex-Amor<sup>a,b</sup>, Ángel Palomares-Caballero<sup>a</sup>, Francisco Mesa<sup>c</sup>, Oscar Quevedo-Teruel<sup>d</sup>, Pablo Padilla<sup>a</sup>

<sup>a</sup>*Departamento de Teoría de la Señal, Telemática y Comunicaciones, Universidad de Granada, 18071 Granada, Spain; e-mail: aalex@ugr.es; angelpc@ugr.es; pablopadilla@ugr.es*

<sup>b</sup>*Information Processing and Telecommunications Center, Universidad Politécnica de Madrid, 28040 Madrid, Spain*

<sup>c</sup>*Microwaves Group, Department of Applied Physics 1, Escuela Técnica Superior de Ingeniería Informática, Universidad de Sevilla, 41012 Sevilla, Spain; e-mail: mesa@us.es*

<sup>d</sup>*Division for Electromagnetic Engineering, School of Electrical Engineering and Computer Science, KTH Royal Institute of Technology, SE-100 44 Stockholm, Sweden; e-mail: oscarqt@kth.se*

## **Keyword:**

Liquid crystal, periodic structures, commercial simulators, dispersion diagram, reconfigurable devices, gap waveguide, microstrip, phase shifter, leaky-wave antenna.

## **Abstract:**

This paper presents an efficient method to compute the dispersion diagram of periodic structures with generic anisotropic media. The method takes advantage of the ability of full-wave commercial simulators to deal with finite structures having anisotropic media. In particular, the proposed method opens new possibilities with respect to commercial eigenmode solvers: (i) anisotropic materials with non-diagonal permittivity and permeability tensors can be analyzed; (ii) the attenuation constant can easily be computed and lossy materials can be included in the simulation; (iii) unbounded and radiating structures such as leaky-wave antennas can be treated. In this work, the proposed method is particularized for the study of liquid crystals (LCs) in microwave and antenna devices. Since LCs show promising capabilities for the design of electronically reconfigurable elements, the dispersion properties of a great variety of LC-based configurations are analyzed, from canonical structures, such as waveguide and microstrip, to complex reconfigurable phase shifters in ridge gap-waveguide technology and leaky-wave antennas. Our results have been validated with previously reported works in the literature and with the Eigenmode solver of commercial software *CST*.

## **1. Introduction**

Periodic structures are commonly used in many fields of science and engineering. By modifying the geometrical parameters of the unit cell, the propagation of electromagnetic waves throughout the structure can easily be tailored. The addition of tunable materials such as graphene [1], ferroelectrics [2] or liquid crystal [3] brings an extra degree of reconfigurability to periodic structures. As an example, the radiation properties of antennas [4, 5, 6] and the phase response of guiding structures [7, 8, 9] can be electronically controlled, as usually demanded to fulfill the technological challenges of last generation communication systems [10].

The dispersion diagram is the usual scenario to analyze the wave propagation in periodic structures [11, 12]. It gives useful information on the phase velocity, attenuation, radiation losses, coupling between high-order modes, etc. Unfortunately, the anisotropic behavior of the vast majority of tunable materials hampers the computation of dispersion diagrams by general-purpose commercial simulators, even for lossless scenarios. Furthermore, the complex nature of the propagation constant (real and imaginary parts) in lossy and/or radiating structures brings an extra difficulty. In this paper, we propose the use of a multi-modal transfer-matrix method to overcome these weaknesses of the frequency-domain eigenmode solvers of common commercial simulators. The proposed methodology is based on the computation of the general transfer matrix and the resolution of an eigenvalue problem derived from a Floquet analysis [13, 14, 15, 16, 17, 18, 19, 20, 21, 12, 22, 23, 24]. In particular, the use of the proposed multi-modal approach offers three main advantages over the eigensolver tools of commercial simulators when analyzing periodic structures with generic anisotropic media:

1. Anisotropic materials with non-diagonal permittivity and permeability tensors can be considered. It should be noted that some commercial simulators deal with anisotropic materials with diagonal tensors, but

fail to account for non-diagonal tensors.

2. Since the attenuation constant can easily be computed, lossy materials can be analyzed with the multi-modal method. This will be exploited in Sec. 5 for the analysis of a reconfigurable phase shifter based on a liquid crystal.

3. Unbounded and radiating structures can be treated, unlike what happens in most commercial simulators where the structure has to be bounded with perfect electric/magnetic conditions. This will be exploited in Sec. 6 for the analysis and optimization of a reconfigurable leaky-wave antenna that uses a liquid crystal as a tunable material.

Liquid crystal is one of the most promising tunable materials for applications in the microwave range [25]. However, the study of the wave propagation in liquid-crystal-based periodic structures is a complex task due to the anisotropic and lossy nature of the material, accounted for by a non-diagonal permittivity tensor [26]. As a consequence, the multi-modal transfer-matrix method arises as an interesting option to analyze periodic structures with liquid crystal material in the design of electronically reconfigurable devices.

The paper is organized as follows. Sec. 2 describes the formulation of the multi-modal transfer-matrix method for periodic structures in general anisotropic media. Then, we particularize to the use of liquid crystal and the main properties of this material are summarized. In Sec. 3 the dispersion properties of rectangular and parallel-plate waveguides filled with liquid crystal are analyzed. Sec. 4 analyzes the dispersion properties of microstrip lines suspended on liquid crystal substrates. The analysis of the dispersion properties of an electrically reconfigurable phase shifter in ridge gap-waveguide technology is carried out in Sec. 5. In Sec. 6 the design of a electrically reconfigurable leaky-wave antenna is discussed. It should be remarked that the results presented in Secs. 3-6 have been validated with previously reported data in the literature and with the Eigenmode solver of *CST*. Finally, the main conclusions of the work are drawn in Sec. 7.

## 2. Theoretical Framework

### 2.1. Multi-modal Analysis

The Multi-Modal Transfer-Matrix Method (MMTMM) applied to the computation of periodic structures in anisotropic media is briefly outlined in this section. For the sake of simplicity, we focus on the study of 1-D periodic structures, although the analysis can be straightforwardly extended to 2-D periodic structures [23, 24].

For a 1-D periodic structure, the eigenvalue problem that leads to the dispersion relation is [12]

$$\mathbf{T} \begin{pmatrix} \mathbf{V} \\ \mathbf{I} \end{pmatrix} = e^{\gamma p} \begin{pmatrix} \mathbf{V} \\ \mathbf{I} \end{pmatrix} \quad (1)$$

where  $\mathbf{T}$  is the  $2N \times 2N$  multi-modal transfer matrix, with  $N$  being the number of modes considered in the computation,  $\mathbf{V}$  and  $\mathbf{I}$  are  $N \times 1$  arrays containing the voltages and currents at the output ports,  $\gamma = \alpha + j\beta$  is the propagation constant,  $\alpha$  is the attenuation constant,  $\beta$  is the phase constant, and  $p$  is the period of the unit cell. The transfer matrix, which is partitioned in four  $N \times N$  submatrices  $\mathbf{A}$ ,  $\mathbf{B}$ ,  $\mathbf{C}$ , and  $\mathbf{D}$  as

$$\mathbf{T} = \begin{pmatrix} \overbrace{\begin{matrix} A^{11} & \dots & A^{1N} \\ \vdots & \ddots & \vdots \\ A^{N1} & \dots & A^{NN} \end{matrix}}^{\mathbf{A}} & \overbrace{\begin{matrix} B^{11} & \dots & B^{1N} \\ \vdots & \ddots & \vdots \\ B^{N1} & \dots & B^{NN} \end{matrix}}^{\mathbf{B}} \\ \overbrace{\begin{matrix} C^{11} & \dots & C^{1N} \\ \vdots & \ddots & \vdots \\ C^{N1} & \dots & C^{NN} \end{matrix}}^{\mathbf{C}} & \overbrace{\begin{matrix} D^{11} & \dots & D^{1N} \\ \vdots & \ddots & \vdots \\ D^{N1} & \dots & D^{NN} \end{matrix}}^{\mathbf{D}} \end{pmatrix} \quad (2)$$

can be derived from the generalized multi-mode scattering matrix  $\mathbf{S}$ , as detailed in [27, 28] or, alternatively, by means of the algebraic manipulations presented, for instance, in [19, Eq. (1)]. Submatrices  $\mathbf{S}_{11}$ ,  $\mathbf{S}_{12}$ ,  $\mathbf{S}_{21}$ ,  $\mathbf{S}_{22}$  relate the  $N$  modes between the input (1) and output (2) ports inside the generalized scattering matrix  $\mathbf{S}$ ,

represented as

$$\mathbf{S} = \begin{pmatrix} \overbrace{\begin{matrix} S_{11}^{11} & \cdots & S_{11}^{1N} \\ \vdots & \ddots & \vdots \\ S_{11}^{N1} & \cdots & S_{11}^{NN} \end{matrix}}^{\mathbf{S}_{11}} & \overbrace{\begin{matrix} S_{12}^{11} & \cdots & S_{12}^{1N} \\ \vdots & \ddots & \vdots \\ S_{12}^{N1} & \cdots & S_{12}^{NN} \end{matrix}}^{\mathbf{S}_{12}} \\ \hline \overbrace{\begin{matrix} S_{21}^{11} & \cdots & S_{21}^{1N} \\ \vdots & \ddots & \vdots \\ S_{21}^{N1} & \cdots & S_{21}^{NN} \end{matrix}}^{\mathbf{S}_{21}} & \overbrace{\begin{matrix} S_{22}^{11} & \cdots & S_{22}^{1N} \\ \vdots & \ddots & \vdots \\ S_{22}^{N1} & \cdots & S_{22}^{NN} \end{matrix}}^{\mathbf{S}_{22}} \end{pmatrix} \quad (3)$$

In the case that the structure under study is symmetrical and reciprocal ( $\mathbf{A} = \mathbf{D}^H$ ,  $\mathbf{B} = \mathbf{B}^H$ ,  $\mathbf{C} = \mathbf{C}^H$ ), the original  $2N$ -rank eigenvalue problem in (1) can be simplified to the  $N$ -rank eigenvalue problem [24]

$$\mathbf{A}\mathbf{V} = \cosh(\gamma p)\mathbf{V}. \quad (4)$$

The multi-modal scattering matrix  $\mathbf{S}$  of a periodic structure can be computed via full-wave simulations of a single unit cell. Inter-cell coupling effects are taken into account through the higher-order modes used in the multi-mode representation [22]. Commercial simulators or in-house codes can be utilized for this purpose. In this work, we make use of the commercial software *CST Microwave Studio* for the extraction of the scattering matrix  $\mathbf{S}$ . It should be remarked that the scattering parameters of finite structures can be computed in anisotropic media (including losses and non-diagonal tensorial materials) with the time-domain and frequency-domain solvers of *CST*. Further technical details are given in the Appendix. However, the dispersion diagrams of the periodic structure cannot directly be computed with the *CST* Eigenmode solver, unless the anisotropic material is lossless and defined by a diagonal tensor. Therefore, the proposed hybrid implementation benefits from the use of commercial simulators to obtain the multi-modal transfer matrix and then compute the dispersion properties of periodic structures in anisotropic media by solving the corresponding eigenvalue problem.

## 2.2. Liquid Crystal

As is well known, liquid crystal (LC) is a state of matter that combines properties of liquids and solid crystals. The elongated rod-like shape of molecules in LCs gives the material its characteristic anisotropic behavior, defined by the fast and slow propagation axes. Depending on the type of order of the molecules, there exist different states or mesophases in which LCs can be found: nematic, smectic and cholesteric [26, 29]. From all the mentioned states, nematic LCs have demonstrated to be particularly useful for the design of reconfigurable radio-frequency devices, such as filters [30, 31, 32], antennas [6, 33, 34, 35], and phase shifters [9, 36, 37]. In a nematic LC, molecules are oriented in the same average direction, represented by the director  $\hat{\mathbf{n}}$  and the average tilt angle  $\theta_m$ . Molecules can be reoriented with the use of magnetic or electric fields [26, 29]. If LCs are enclosed between metallic plates, which could be the case of waveguides, parallel plates and microstrip lines (see Fig. 1), quasi-static electric fields are normally used for simplicity to polarize the material. Molecules tend to orient parallel to the metallic plates when a low-intensity electric field is applied [Fig. 1(a)] whereas molecules orient perpendicular to the metallic plates when a high-intensity electric field is applied [Fig. 1(b)].

The uniaxial permittivity tensor that characterizes the electrical properties of the LC can be expressed as [3, 26]

$$\bar{\epsilon} = \begin{pmatrix} \epsilon_{\perp} & 0 & 0 \\ 0 & \epsilon_{\perp} + \Delta\epsilon \cos^2 \theta_m & \Delta\epsilon \cos \theta_m \sin \theta_m \\ 0 & \Delta\epsilon \cos \theta_m \sin \theta_m & \epsilon_{\perp} + \Delta\epsilon \sin^2 \theta_m \end{pmatrix} \quad (5)$$

where  $\Delta\epsilon = \epsilon_{\parallel} - \epsilon_{\perp}$  is the dielectric anisotropy,  $\epsilon_{\parallel}$  is the parallel permittivity and  $\epsilon_{\perp}$  is the perpendicular permittivity. The loss tangent tensor is calculated analogously, by replacing  $\Delta\epsilon$  and  $\epsilon_{\perp}$  in (5) by the anisotropic loss tangent  $\Delta \tan \delta = \tan \delta_{\parallel} - \tan \delta_{\perp}$  and the perpendicular loss tangent  $\tan \delta_{\perp}$ , respectively. As previously stated,  $\theta_m$  represents the average tilt angle of the molecules. This angle is a function of the elastic constants  $k_{ii}$  [38], the dielectric anisotropy at the bias frequency  $\Delta\epsilon^b$ , the intensity of the quasi-static electric field and the pretilt angle  $\theta_p \simeq 0$ . That is,  $\theta_m = \theta_m(k_{11}, k_{22}, k_{33}, \Delta\epsilon^b, V, \theta_p)$ . A detailed study particularized to LCs enclosed in parallel-plate waveguides, showing the relation between  $\theta_m$  and the parameters presented above, can be found in [39, 40].

The permittivity tensor (5) becomes a diagonal tensor for the extreme cases of  $\theta_m = 0^\circ$  and  $\theta_m = 90^\circ$ , when the LC is polarized with  $V = 0$  V (with  $\theta_p = 0$ ), and an hypothetical infinite voltage  $V_{\infty}$ , respectively.

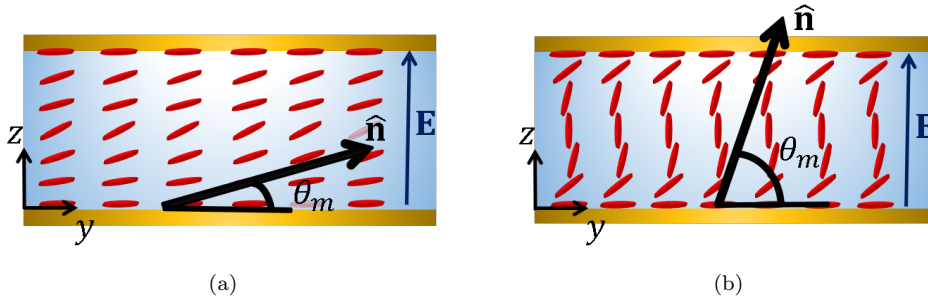


Figure 1: Molecular reorientation in a nematic liquid crystal enclosed by two metallic plates when a (a) low-intensity and (b) high-intensity quasi-static electric field  $\mathbf{E}$  is applied. Unit vector  $\hat{\mathbf{n}}$  represents the average director and  $\theta_m$  the average tilt angle.

As previously discussed, eigensolver tools of commercial simulators can usually only compute the dispersion properties of anisotropic materials with diagonal permittivity and permeability tensors. As a consequence, only these two particular lossless cases can directly be treated by them. The present study extends the analysis of periodic structures involving liquid crystals to all intermediate cases, where the permittivity tensor presents a non-diagonal form. Furthermore, losses can be included in the computation.

### 3. Metallic Waveguide

The study of metallic waveguides filled with skew uniaxial dielectrics has been a topic of continuous interest in microwave/antennas engineering [41, 42, 43]. It is well known that, in general, these waveguides support hybrid modes, and only in some particular cases there exist pure TE/TM modes in the waveguide. In our LC case under study, given the structure of the permittivity tensor in (5), the modes of the LC-filled waveguide will be hybrid when  $\theta_m \neq 0, 90$ , thus requiring the MMTMM to obtain accurate solutions. Here it should be noted that, although the MMTMM is originally posed to deal with periodic structures, it can also be applied to the computation of the dispersion diagram of uniform (non-periodic) structures. This computation is found sufficiently accurate provided that the phase shift,  $\beta L$ , is not close to the edges of the first Brillouin zone, where  $L$  is the length of the considered waveguide section. It is then advisable to use small values of  $L$  when computing the scattering parameters of the waveguide in the commercial simulator.

Before studying the LC-filled waveguides, a validation of the method will be carried out by comparing the results reported in [42, Table I] for a metallic waveguide filled with a strongly anisotropic skew uniaxial dielectric with the ones provided by the MMTMM. This comparison is shown in Table 1, where our results with  $N = 1$  means that only the  $\text{TE}_{10}$  is employed in the input/output port,  $N = 2$  stands for an additional  $\text{TE}_{01}$  mode, and  $N = 3$  for an additional  $\text{TE}_{21}$  mode. This consecutive addition of modes follows the rationale in [42] for the first, second, and third approximations there discussed. In particular, the column data from [42] in the table correspond to the third approximation. Our results show a good convergence as  $N$  increases as well as a good agreement with those from [42]. As commented in [42], the skew anisotropy actually requires the hybrid modal solutions of the waveguide to be constructed in general with multiple TE and TM modes (the required number to achieve accuracy will depend on the operation frequency). However, in situations where the off-diagonal elements of the permittivity tensors are smaller than the diagonal ones, the number of required modes could be reduced to a pair of modes or even just a single mode.

Once the MMTMM has been conveniently validated, it will be used to analyze the dispersion properties of a uniform metallic waveguide (along the  $x$ -direction) filled with a LC. Fig. 2 shows the dispersion diagram of

Table 1: Guide wavelength,  $\lambda_g$ , as a function of the free-space wavelength,  $\lambda_0$ , both in mm, for the test case presented in [42]

| $\lambda_0$ | $N = 1$ | $N = 2$ | $N = 3$ | [42]    |
|-------------|---------|---------|---------|---------|
| 7           | 0.6512  | 0.5886  | 0.5878  | 0.5852  |
| 8.5         | 0.8525  | 0.7953  | 0.7948  | 0.7932  |
| 10          | 1.1410  | 1.0787  | 1.0756  | 1.0680  |
| 12          | 1.8487  | 1.7782  | 1.7573  | 1.6496  |
| 15          | j3.6047 | j4.9223 | j4.9478 | j5.0090 |

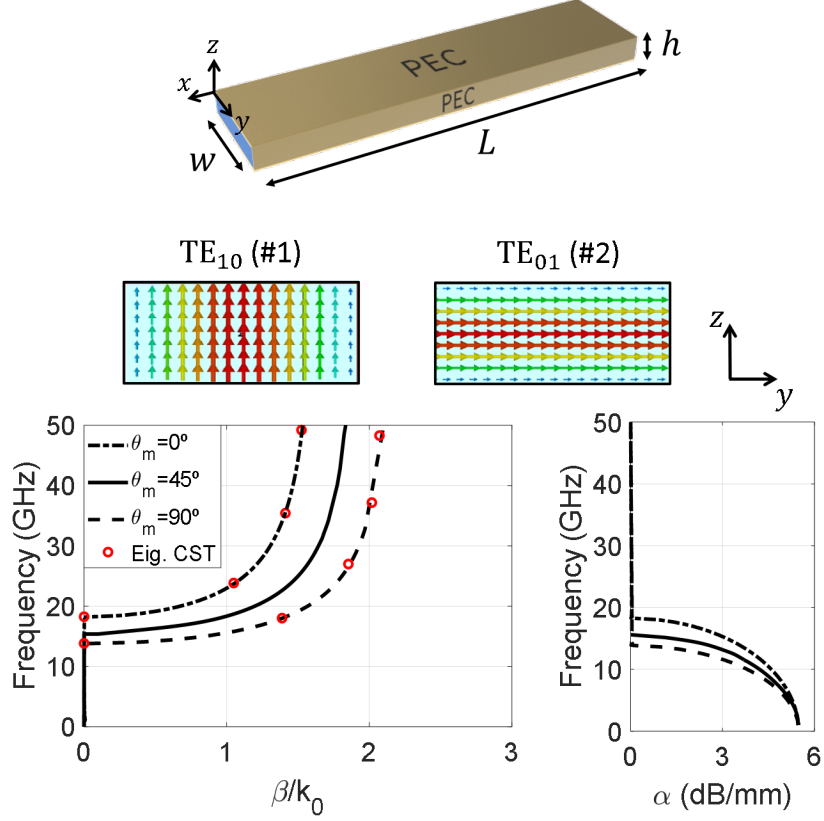


Figure 2: Dispersion diagram of a metallic rectangular waveguide filled with lossless liquid crystal.  $N = 2$  modes have been used for the computation of the hybrid mode. The electrical and geometrical parameters of the liquid crystal cell are:  $\epsilon_{\perp} = 2.7$ ,  $\Delta\epsilon = 2$ ,  $L = 0.01$  mm,  $w = 5$  mm,  $h = 2.5$  mm.

both the phase ( $\beta$ ) and attenuation ( $\alpha$ ) constants for different values of the average orientation of the molecules in the LC. When  $\theta_m = 0, 90$ , the permittivity tensor is diagonal and, according to [42, 43], pure TE and TM modes exist. In particular, when the optic axis is oriented along the  $y$  axis ( $\theta_m = 0$ ), the fundamental mode is the  $\text{TM}_{Y10}$ , following the notation of [43]. When the optic axis is oriented along the  $z$  axis ( $\theta_m = 90$ ), the fundamental mode is the  $\text{TE}_{Z10}$ . Both  $\text{TM}_{Y10}$  and  $\text{TE}_{Z10}$  modes have correspondence with the  $\text{TE}_{10}$  mode in a conventional waveguide loaded with an homogeneous isotropic dielectric [43]. This means that only one mode ( $N = 1$ ) is required in the MMTMM to obtain accurate results in both  $\theta_m = 0, 90$  cases. In fact, an excellent agreement is observed in Fig. 2 between the proposed method and the Eigenmode solver of *CST* for these cases. Note that the structure becomes denser (high values of  $\beta/k_0$ ) as the average tilt angle  $\theta_m$  increases. This is due to the effective permittivity of the LC is mainly influenced by the term  $\epsilon_{zz}$  of the permittivity tensor, since the electric field is mostly oriented along  $z$  axis. As already commented, only the phase constant of these two extreme cases can be computed with the Eigenmode solver of the commercial simulator, corresponding to the situations in which the tensor is diagonal and no losses are considered. The Eigenmode solver of *CST* cannot compute the attenuation constant in periodic structures, not even in lossless and bounded isotropic scenarios. However, information of the attenuation constant in the passband and stopband regions is relevant from a practical point of view, especially in liquid crystals due to their intrinsic lossy nature. The proposed multi-modal approach can help us in these situations, providing accurate results for both phase and attenuation constants in all polarization states of the LC. In the case shown in Fig. 2 for  $\theta_m = 45$ ,  $N = 2$  modes in the input/output ports suffice to achieve convergence in the considered frequency range; namely, the  $\text{TE}_{10}$  and the  $\text{TE}_{01}$  modes.

#### 4. Microstrip-like Line

Previous works have reported complex numerical techniques to study the wave propagation in microstrip lines filled with liquid crystal [44, 45]. In this section, we show that the dispersion properties of a LC-based microstrip-

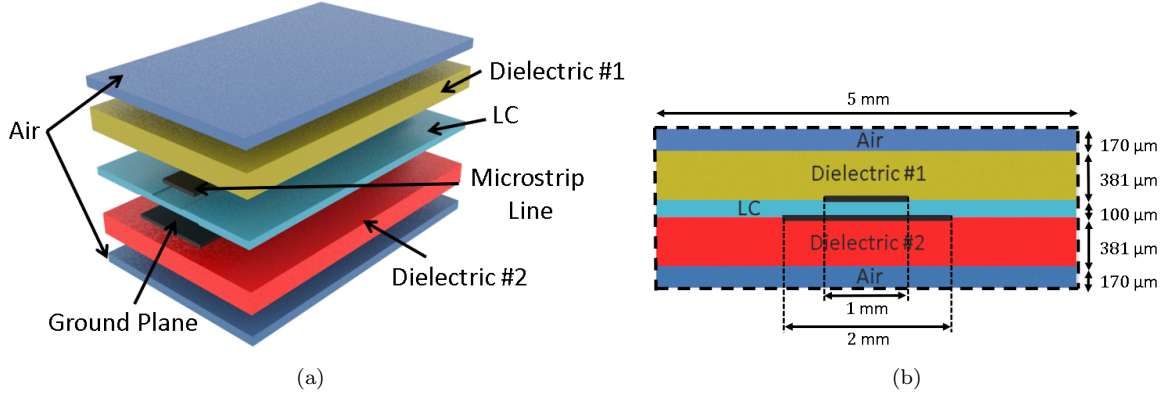


Figure 3: Microstrip section filled with liquid crystal presented in [44]: (a) 3-D view, (b) transversal cut.

like line can be analyzed in an alternative and easier manner with the use of the MMTMM. Specifically, the structure analyzed in [44] is now analyzed with the MMTMM and the results compared with measurement and numerical (Finite Elements Method, FEM) data provided in [44].

A 3-D view of the microstrip structure under study is depicted in Fig. 3(a) with Fig. 3(b) showing a transversal cut with the different layers and dimensions. A Merck E7 liquid crystal of electrical parameters  $\varepsilon_{\perp} = 2.78$ ,  $\Delta\varepsilon = 0.47$ ,  $k_{11} = 11.1$  pN,  $k_{22} = 10.0$  pN,  $k_{33} = 17.1$  pN,  $\theta_p = 2^\circ$  and  $\Delta\varepsilon^b(1 \text{ kHz}) = 13.8$  was chosen in [44]. Note that the elastic constants  $k_{ii}$ , the pretilt angle  $\theta_p$  and the dielectric anisotropy at the bias frequency  $\Delta\varepsilon^b$  (see Sec. 2.2) are given in this case to relate a determined polarization voltage  $V$  with the resulting average tilt angle  $\theta_m$ . Two dielectrics of permittivity  $\varepsilon_r^{\text{diel1}} = 3.27$ , and  $\varepsilon_r^{\text{diel2}} = 9.8$  are used to encapsulate the LC. For the computation, the length of the microstrip section is  $L = 1$  mm. As in [44], the structure is shielded by applying electric to the edges of Fig. 3(b), represented by black dashed lines.

The dispersion diagram of the lossless LC-based microstrip section presented in [44] is shown in Fig. 4 for different polarization voltages. In our computations with the MMTMM, it is found that the use of just the fundamental propagating qTEM mode ( $N = 1$ ) suffices to provide accurate enough results. This is confirmed with the good agreement found with the results extracted from the Eigenmode solver of *CST* as well as the obtaining of a negligible attenuation constant ( $\alpha/k_0 < 5 \times 10^{-3}$ ) in all the considered frequency range. Additionally, it should be remarked that a null polarization voltage ( $V = 0$ ) does not represent in this particular case a diagonal tensor, since the pretilt angle is different from zero ( $\theta_p = 2$ ) here. Thus, the average tilt angle associated with a null polarization voltage will be approximately  $\theta_m \approx \theta_p = 2$ , resulting in a non-diagonal tensor. As a consequence, the *CST* Eigenmode solver cannot actually compute the case  $V = 0$ , although it can be approximated with almost negligible error to a diagonal tensor ( $\theta_m \approx 0$ ).

In order to form the permittivity tensor (5) and then compute the S-parameters of the structure in *CST*, a conversion between the polarization voltage  $V$  and the average tilt angle  $\theta_m$  has to be done. This conversion has been carried out with the formulas of [40], originally intended for application in parallel-plate waveguides. If fringing-field effects are neglected, the formulas of [39, 40] approximate well the relation between  $V$  and  $\theta_m$  in microstrip structures. Looking at the phase constant in Fig. 4, it can be appreciated that the structure becomes denser as the polarization voltage increases. Furthermore, the LC is almost saturated (with respect to  $V_\infty$ ) for a very low voltage values such as  $V = 2$  V due to the elevated dielectric anisotropy  $\Delta\varepsilon^b$  that Merck E7 LC possesses at the bias frequency. Note that the higher  $\Delta\varepsilon^b$  is, the lower the voltage value needed to approach the theoretical limit imposed by  $V_\infty$ .

In Fig. 5, the relative effective permittivity of the structure at 60 GHz is shown for different polarization voltages. This permittivity is computed as  $\varepsilon_{r,\text{eff}}(f) = \beta^2(f)/k_0^2(f)$ , which is directly extracted from the dispersion diagrams in Fig. 4. An excellent agreement is observed with the FEM and measurement data reported in [44]. As previously discussed, the effective permittivity rapidly saturates for low polarization voltages due to the elevated dielectric anisotropy at the bias frequency. Note that the maximum effective relative permittivity would be approximately  $\varepsilon_{r,\text{eff}} \approx \varepsilon_{\parallel} = 3.25$  for  $V \rightarrow \infty$ , and that  $\varepsilon_{r,\text{eff}}(V = 8 \text{ V}) = 3.18$  is already close to this value.

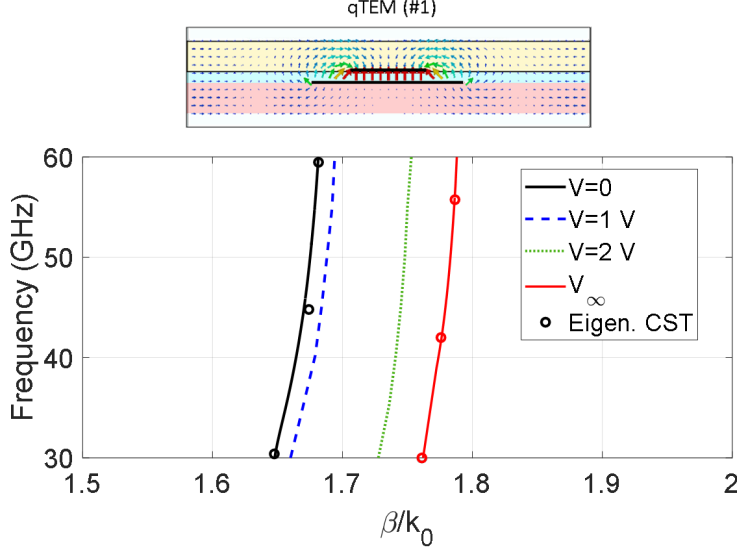


Figure 4: Dispersion diagram of the lossless microstrip-like line with a liquid crystal cell presented in [44] for the extreme and some intermediate polarization stages ( $N = 1$  mode). The electrical field distribution of the considered mode is shown in the figure. The electrical parameters of the liquid crystal cell and dielectrics are  $\varepsilon_{\perp} = 2.78$ ,  $\Delta\varepsilon = 0.47$ ,  $k_{11} = 11.1$  pN,  $k_{22} = 10.0$  pN,  $k_{33} = 17.1$  pN,  $\theta_p = 2^\circ$ ,  $\Delta\varepsilon^b(1 \text{ kHz}) = 13.8$ ,  $\theta_p = 2^\circ$ ,  $\varepsilon_r^{\text{diel1}} = 3.27$ , and  $\varepsilon_r^{\text{diel2}} = 9.8$ .

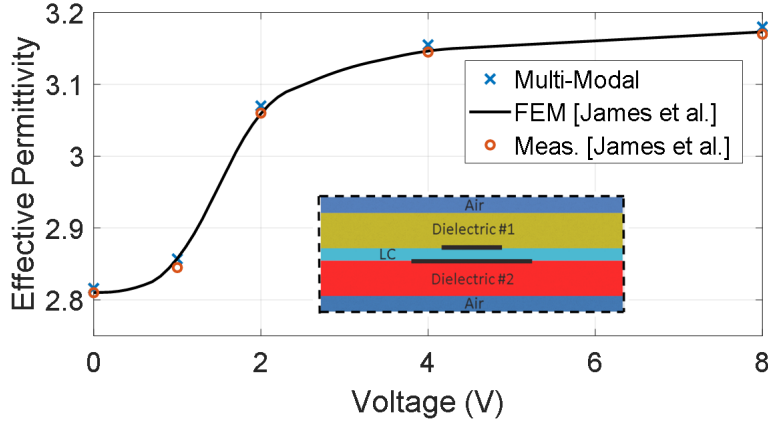


Figure 5: Effective relative permittivity at 60 GHz for different polarization voltages. A comparison is made with the numerical results and measurements presented in [44].  $N = 1$  mode is used for the computation. The electrical parameters of the liquid crystal cell and dielectrics are  $\varepsilon_{\perp} = 2.78$ ,  $\Delta\varepsilon = 0.47$ ,  $k_{11} = 11.1$  pN,  $k_{22} = 10.0$  pN,  $k_{33} = 17.1$  pN,  $\theta_p = 2^\circ$ ,  $\Delta\varepsilon^b(1 \text{ kHz}) = 13.8$ ,  $\theta_p = 2^\circ$ ,  $\varepsilon_r^{\text{diel1}} = 3.27$ , and  $\varepsilon_r^{\text{diel2}} = 9.8$ .

## 5. Reconfigurable Phase Shifter

In this section we present the design and analysis of a LC-based reconfigurable phase shifter in ridge gap-waveguide technology. The dispersion properties of the reconfigurable phase shifter in lossless and lossy scenarios are computed by means of the MMTMM. This task could be of potential interest for the development of efficient tunable phase shifters applied to the design of phased array antennas.

An schematic of the phase shifter in ridge gap-waveguide technology and its transversal cut view are shown in Figs. 6(a) and (b), respectively. Waves ideally propagate inside the LC between the two metallic parallel plates that form the ridge and the upper plate. The phase shift is then electronically controlled by polarizing the LC and changing the orientation of the molecules. Similarly to the design recently proposed in [36], a container made of Rexolite is employed to confine the LC and prevent its leakage. The bed of nails inserted at both sides of the liquid crystal acts as an artificial magnetic conductor (AMC), creating a high impedance surface condition. For computation purposes, an LC mixture GT3-23001 has been used:  $\varepsilon_{\perp} = 2.46$ ,  $\Delta\varepsilon = 0.82$ ,  $\tan \delta_{\perp} = 0.0143$ ,  $\tan \delta_{\parallel} = 0.0038$ , and Rexolite of electrical parameters  $\varepsilon_r^{\text{Rexo}} = 2.33$  and  $\tan \delta^{\text{Rexo}} = 0.00066$ .



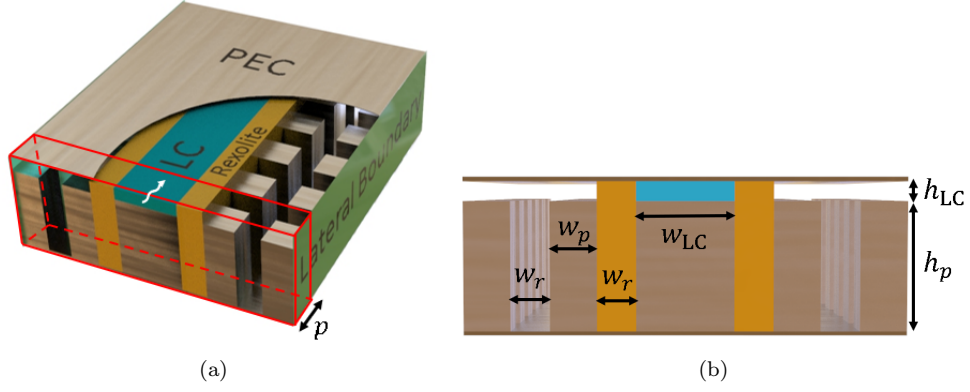


Figure 6: Liquid-crystal-based reconfigurable phase shifter in ridge gap-waveguide technology.

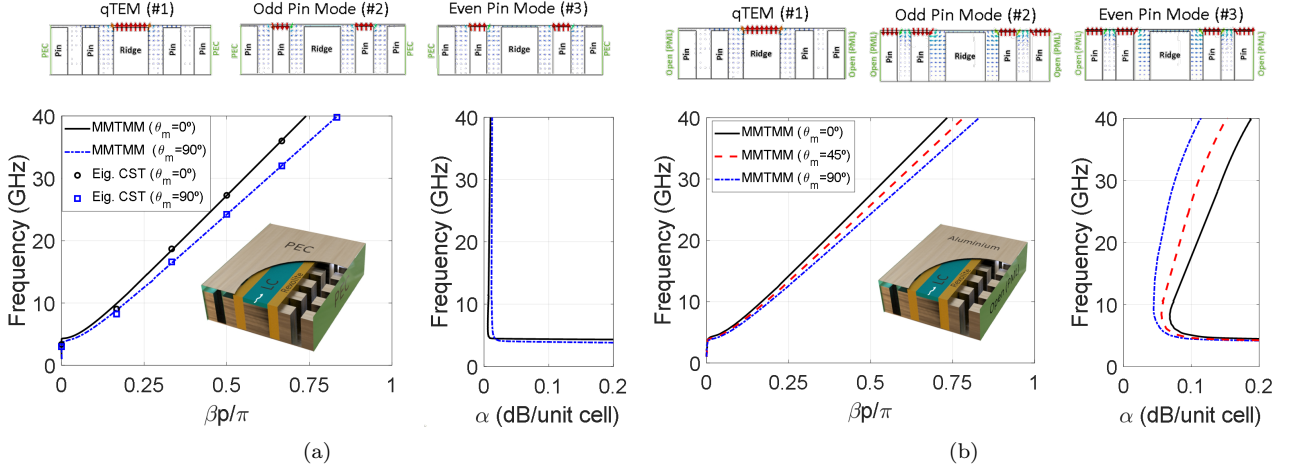


Figure 7: Dispersion diagram of a (a) lossless and (b) lossy ridge gap waveguide phase shifter filled with liquid crystal. The results are obtained with  $N = 3$  modes. The electric field distribution of the three considered modes is displayed in the figure. The electrical and geometrical parameters of the unit cell are:  $\epsilon_{\perp} = 2.46$ ,  $\Delta\epsilon = 0.82$ ,  $\tan\delta_{\perp} = 0.0143$ ,  $\tan\delta_{\parallel} = 0.0038$ ,  $\epsilon_r^{\text{Rexo}} = 2.33$ ,  $\tan\delta^{\text{Rexo}} = 0.00066$ ,  $p = 1.76$  mm,  $w_{LC} = 2$  mm,  $h_{LC} = 80$   $\mu\text{m}$ ,  $w_p = 0.96$  mm,  $h_p = 2.64$  mm, and  $w_r = 0.8$  mm.

[36].

Figs. 7(a) and (b) show the dispersion diagrams of the reconfigurable phase shifter in lossless and lossy scenarios, respectively, for different average tilt angles  $\theta_m$ . Both diagrams have been computed with  $N = 3$  modes. The electric field distributions of the three modes considered in the input/output ports are displayed in the figures. Note that modes #2 and #3 are included to take into account wave propagation along the pins and ensure a correct convergence of the method. The cutoff frequency of the propagating quasi-TEM mode (as it is usually called in ridge gap waveguides [46]), located approximately at 2.95 GHz, is evidenced in both subfigures. Below the cutoff, even and odd quasi-TEM modes can propagate between the pins and the upper metal plate with a high attenuation constant [46].

In Fig. 7(a), the values of the phase and attenuation constants computed with the MMTMM in a lossless and bounded (PEC as lateral boundaries) structure are shown and compared with the data provided by the *CST* Eigenmode solver. A good agreement is found between both set of results. Although the qTEM mode should have a null attenuation constant ( $\alpha = 0$ ) in the propagating frequency range (due to the absence of losses), small values of attenuation appear in the MMTMM due to inevitable numerical noise. Fig. 7(b) presents a more realistic scenario, where the phase and attenuation constants are computed in a lossy and open (PML as lateral boundaries) structure. Material losses have been included in the liquid crystal and in the Rexolite, and PEC layers have been replaced by aluminium. As the *CST* Eigenmode solver does not provide the dispersion diagram in lossy and open structures, no comparison with *CST* appears in Fig. 7(b). Three different values of  $\theta_m$  have been considered: 0, 45 and 90. The structure becomes denser as  $\theta_m$  increases as a consequence



of the corresponding increment of the the effective permittivity of the LC. Also, it is observed a progressive increase of the attenuation constant as frequency increases, associated with the longer electrical length that the wave has to travel at higher frequencies. The case  $\theta_m = 0$  shows the highest attenuation constant, since for this configuration the effective term of the loss tangent tensor (due to the orientation of the electric field) is  $\tan \delta_{zz} = \tan \delta_{\perp}$ , which has a value greater than  $\tan \delta_{\parallel}$ . Conversely, the case  $\theta_m = 90^\circ$  presents a lower attenuation constant, since the effective term of the loss tangent tensor is  $\tan \delta_{zz} = \tan \delta_{\parallel}$  in this configuration and  $\tan \delta_{\parallel} < \tan \delta_{\perp}$ . The case  $\theta_m = 45^\circ$  is an intermediate state in terms of losses.

## 6. Reconfigurable Leaky-Wave Antenna

In this section, the MMTMM is applied to the analysis and design of a reconfigurable leaky-wave antenna (LWA) based on the use of liquid crystal. For validation purposes, we replicate and analyze the design presented in [47], which is one of the few LC-based LWAs reported in the literature that has been manufactured and experimentally measured. Fig. 8 shows the schematic of the LWA; namely, a composite right/left-handed (CRLH) LWA implemented in microstrip technology, the substrate of which is a LC to provide reconfigurability. The radiation angle of the LWA is controlled by polarizing the LC and, therefore, changing the average orientation of the molecules ( $\theta_m$ ). To confine the LC and prevent its leakage, there is a groove on the metal base forming a cavity [see Fig. 8(b)] in combination with a dielectric slab above the LC. The geometrical parameters of the LC-based LWA are given in Table 2. The LC utilized here is TUD-649 ( $\epsilon_{\perp} = 2.46$ ,  $\Delta\epsilon = 0.82$ ) and the dielectric slab has a relative permittivity  $\epsilon_r^{\text{diel}} = 3.66$  [47].

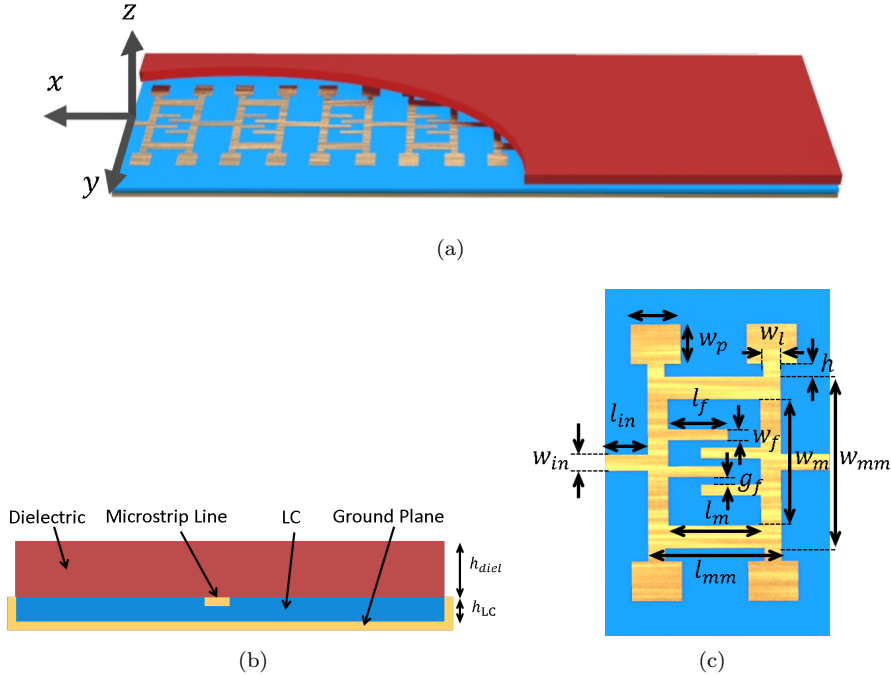


Figure 8: (a) Liquid-crystal-based reconfigurable leaky-wave antenna presented in [47]. (b) Transversal cut view showing its forming layers. (c) Unit cell.

Table 2: GEOMETRICAL PARAMETERS OF THE LC-BASED LWA.

| Parameters | $l_m$    | $w_m$ | $l_{mm}$ | $w_{mm}$ | $l_{in}$   |
|------------|----------|-------|----------|----------|------------|
| Value (mm) | 4        | 6.5   | 2.8      | 4.8      | 1.4        |
| Parameters | $h$      | $w_l$ | $l_p$    | $w_p$    | $l_f$      |
| Value (mm) | 0.5      | 0.5   | 1.5      | 1.5      | 1.8        |
| Parameters | $w_{in}$ | $w_f$ | $g_f$    | $h_{LC}$ | $h_{diel}$ |
| Value (mm) | 0.6      | 0.4   | 0.3      | 0.25     | 0.762      |

### 6.1. Dispersion diagram and radiation properties

Fig. 9 shows the 3-D radiation patterns of the LC-based LWA at different frequencies for the extreme polarization voltages  $V = 0$  ( $\theta_m = 0^\circ$ ) and  $V \rightarrow \infty$  ( $\theta_m = 90^\circ$ ). For computational purposes, six unit cells are concatenated and the Time Domain solver of *CST* is used. As shown, the antenna is able to radiate at broadside direction [12.60 GHz in Fig. 9(a) and 11.60 GHz in Fig. 9(b)] due to the capacitance of the interdigitated structure placed at the center of the unit cell and the shunt inductance obtained by the stub lines connected to the square patches [see Fig. 8(c)]. Below and above the broadside frequency, the antenna scans in backward (BW) and forward (FW) radiation angles.

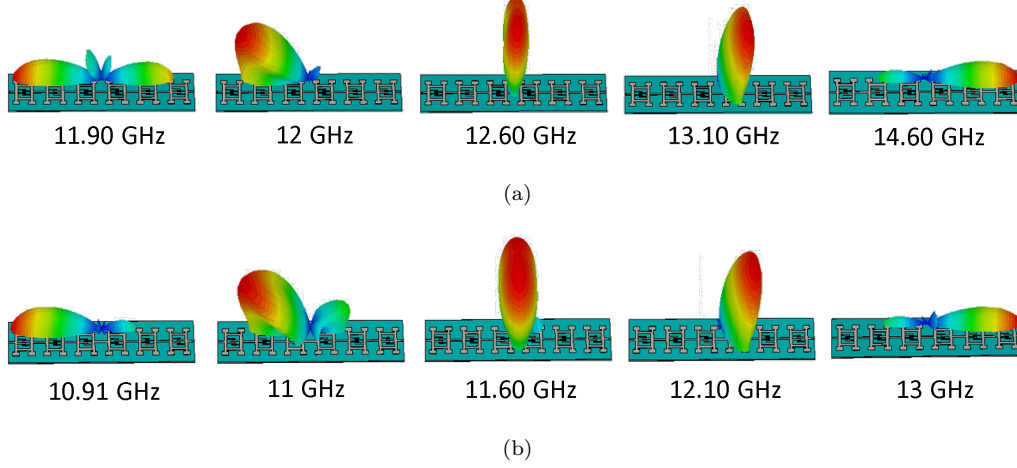


Figure 9: 3-D radiation pattern of the liquid-crystal-based reconfigurable leaky-wave antenna presented in [47] for (a)  $V = 0$  and (b)  $V \rightarrow \infty$  at different frequencies. Input and output ports are located on the left and right side of the structure, respectively.

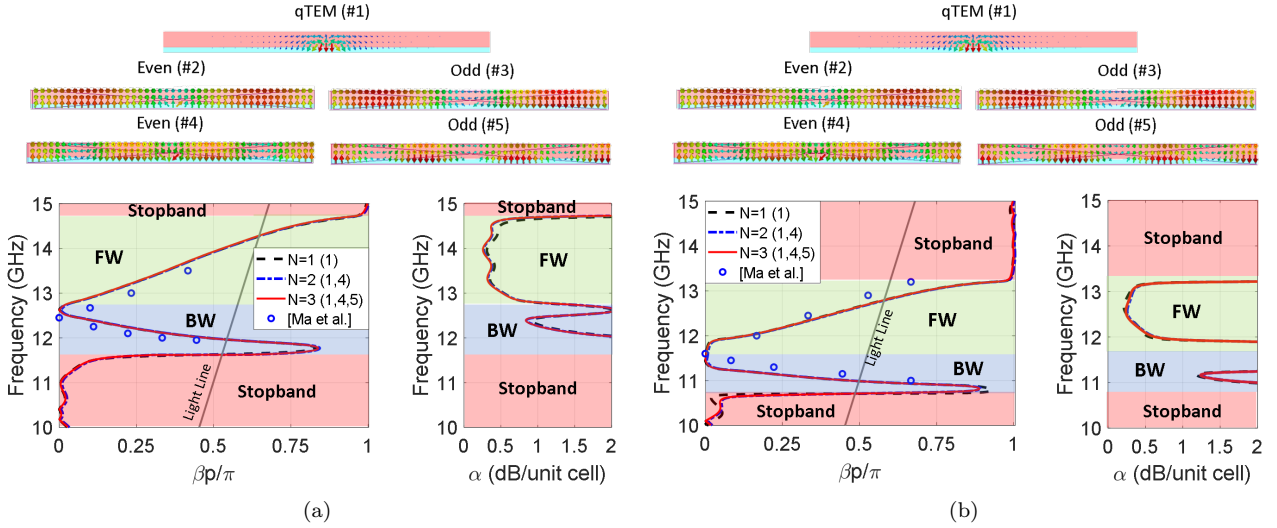


Figure 10: Dispersion diagrams of the liquid-crystal-based reconfigurable leaky-wave antenna presented in [47] for (a)  $V = 0$  and (b)  $V \rightarrow \infty$ . The electrical parameters of the LC are:  $\epsilon_{\perp} = 2.43$ ,  $\Delta\epsilon = 0.79$ .

The dispersion diagrams of the lossless LC-based LWA are shown in Figs. 10(a) and (b) when a null and a hypothetical infinite voltage is applied to the LC, respectively. The results extracted from the MMTMM are in good agreement with the data provided in [47]. Since the structure is not symmetric, it is expected that modes of even and odd parity are required to ensure the convergence of the attenuation and phase constants. In this case, two modes ( $N = 2$ ) are required to achieve that convergence. The combination of modes in the input/output ports that provides the best results includes the modes #1, #4, and #5 depicted in the top panel of Fig. 10. The results in this figure show that mode #4 has relevance in the computation, due to its even nature and the high field intensity near the area of the microstrip line where the qTEM mode propagates. Modes #2 and #3 strongly depend on the size of the *bounded* input/output ports and, therefore, are hardly correlated to the Floquet modes that can physically propagate in the *unbounded* periodic structure. Backward,

forward, and stopband regions are shadowed in Fig. 10. In Fig. 10(a), the broadside frequency (corresponding to  $\beta = 0$ ) is observed at 12.65 GHz, which is in good agreement with the central frequency of the 3-D pattern displayed in Fig. 9(a). At 11.97 GHz, the light line crosses the backward mode ( $\beta = -k_0$ ). This frequency point is associated to backfire radiation in the antenna, which is also evidenced in Fig. 9(a) at 11.90 GHz. Furthermore, note that the reduced slope of the phase constant in the backward region indicates that the scan angle rapidly changes in Fig. 9(a) from backfire to broadside radiation. On the contrary, the slope of the phase constant is higher in the forward region, which indicates a large scanning bandwidth. At 14.35 GHz, the light line crosses the forward mode ( $\beta = k_0$ ). This frequency point is associated with endfire radiation in the antenna, which can be observed at 14.60 GHz in Fig. 9(a). In Fig. 10(b), backfire, broadside, and endfire frequencies are located at 11 GHz, 11.60 GHz, and 12.80 GHz, respectively, in good agreement with the radiation patterns shown in Fig. 9(b).

## 6.2. Optimization of the LWA via the Multi-modal Technique

As it is well known, the radiation efficiency of the antenna is determined by its impedance matching level as well as its leakage rate; namely, the level of reflections of the antenna and the attenuation constant ( $\alpha$ ) of the leaky mode, respectively. Near the broadside frequency, the antenna shows a good matching and, therefore, the attenuation constant accounts well for the radiated power. Since low values of  $\alpha$  are observed in Figs. 9(a) and (b) near the broadside frequency, especially for  $V = 0$ , the radiation efficiency of the LWA is low (taking into consideration that no losses are included in the computation). Unfortunately, no information about the radiation efficiency or the antenna gain is provided in [47].

Next, the MMTMM is used as a design tool to increase the leakage rate and, therefore, the radiation efficiency of the antenna. The results of this study led us to the geometrical parameters of the optimized leaky-wave antenna shown in Table 3. To make a fair comparison, the original shape of the unit cell and thicknesses of the LC and dielectric have been preserved; that is, no additional microstrip sections have been added to the unit cell. The dispersion diagram of the optimized LWA is shown in Fig. 11(a). It can be observed in that figure that the phase constant of the optimized antenna shows a similar behavior as the original antenna and, consequently, the radiation angles of both antennas are similar. However, the leakage rate  $\alpha$  has been enhanced considerably, specially in the forward region, which directly translates in a higher efficiency of the optimized antenna. This fact is evidenced in Fig. 11(b), where the radiation efficiencies of the original and optimized antennas are compared. The radiation efficiency is improved an 11% in the forward region and kept similar in the backward region. The drop in the efficiency observed around 12.5 GHz in Fig. 11(b) for both antennas can be related to the appearance of the so-called open stopbands [48, 49]. This stopband appears in many periodic LWAs when the beam is scanned through broadside and gives rise to peaks in the attenuation constant, as the ones appearing in Fig. 11(a) around 12.7 GHz. The frequency shift found between the efficiency drop in Fig. 11(b) and the attenuation peaks in Fig. 11(a) is associated with the finite size (eight cells) of the periodic LWA analyzed in Fig. 11(b) versus the infinite nature of the periodic structure considered in the dispersion diagram of Fig. 11(a). A parametric study revealed that the open stopband, in agreement with the rationale reported in [48, 49], cannot be easily suppressed with the current configuration of the unit cell. A modified configuration of the antenna would be needed, which could be conveniently analyzed by means of the proposed MMTMM.

Table 3: GEOMETRICAL PARAMETERS OF THE OPTIMIZED LWA.

| Parameters | $l_m$    | $w_m$ | $l_{mm}$ | $w_{mm}$ | $l_{in}$   |
|------------|----------|-------|----------|----------|------------|
| Value (mm) | 4.5      | 6.5   | 2.9      | 5.4      | 0.75       |
| Parameters | $h$      | $w_l$ | $l_p$    | $w_p$    | $l_f$      |
| Value (mm) | 0.6      | 0.5   | 1.55     | 1.55     | 1.8        |
| Parameters | $w_{in}$ | $w_f$ | $g_f$    | $h_{LC}$ | $h_{diel}$ |
| Value (mm) | 0.55     | 0.4   | 0.3      | 0.25     | 0.762      |

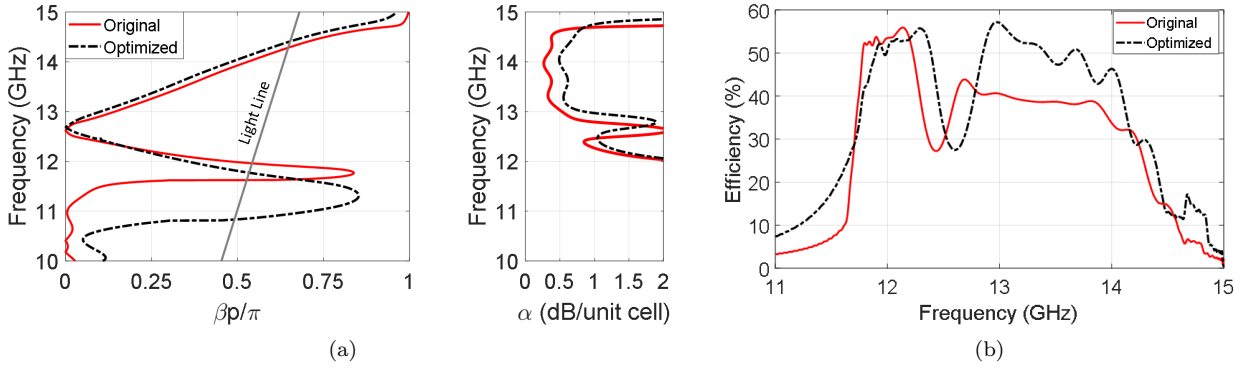


Figure 11: (a) Dispersion diagram of the optimized LC-based leaky-wave antenna for  $V = 0$ . (b) Radiation efficiency of the optimized antenna for  $V = 0$  when 8 unit cells are cascaded. The electrical parameters of the LC are:  $\varepsilon_{\perp} = 2.43$ ,  $\Delta\varepsilon = 0.79$ .

## 7. Conclusion

The use of the multi-modal transfer-matrix method to compute the dispersion diagram of periodic structures involving general anisotropic media has been discussed in this work. We have particularized the study to the case of liquid crystals due to its promising properties for the design of electronically reconfigurable devices. The proposed method, which combines the use of commercial simulators and analytical post-processing, overcomes the main limitations of commercial eigenmode solvers when dealing with anisotropic materials. Specifically, the proposed multi-modal method shows three interesting properties:

1. Anisotropic materials with non-diagonal permittivity and permeability tensors can be analyzed. This is an interesting feature that has been exploited throughout the text, since only the extreme polarization states  $V = 0$  and  $V \rightarrow \infty$  in LC could be typically computed with commercial eigenmode solvers.
2. The attenuation constant can be easily computed. This is of capital relevance in order to analyze the stopband regions of periodic structures. Furthermore, the method allows to include lossy materials in the computation. This is a very appreciated feature in LC-based structures in order to take into account the lossy nature of the material.
3. Unbounded and radiating structures can be analyzed. Conversely, in most of commercial eigenmode solvers the structure must be forcefully shielded with perfect electric/magnetic boundary conditions. This fact prevents that periodic leaky wave antennas can be typically analyzed in commercial softwares.

Some relevant works in the literature were selected to test the method. We started with the study of canonical waveguide and microstrip sections. Afterwards, we apply the multi-modal method to analyze the dispersion properties (phase shift, radiation angle, leaky rate, etc.) of more advanced designs, such as a reconfigurable phase shifter in ridge gap-waveguide technology and a leaky-wave antenna. All results were in good agreement with previously reported works and with the Eigenmode solver of *CST*, demonstrating that the multi-modal method has potential application in the analysis and design of periodic structures that includes liquid crystal or others anisotropic materials.

## Acknowledgments

This work was supported by the Spanish Research and Development National Program under Projects TIN2016-75097-P, RTI2018-102002-A-I00, B-TIC-402-UGR18 and the predoctoral grant FPU18/01965; by Junta de Andaluca under project P18-RT-4830; and by the Spanish Government under Salvador de Madariaga fellowship PRX19/00025 and Project TEC2017-84724-P.

## Appendix A. Technical Details for the Computation of the S-parameters of a Single Unit Cell

In this appendix, the details associated with the computation of the S-parameters of a single unit cell are described. As detailed in Sec. 2.1, the S-parameters can be computed via full-wave simulations with either in-house codes or commercial simulators. In this work, we take advantage of the ability of commercial software *CST Microwave Studio* to deal with arbitrary geometries and materials.

When dealing with anisotropic media in *CST*, two kind of solvers can be utilized to compute the scattering parameters of a single unit cell. Below are detailed the main characteristics of the two type of solvers. These characteristics are referred to version *CST* 2020, the one used in this work, and can differ for other versions.

1. *Time-domain solver*: As it can only deal with diagonal tensors in the simulation, only the extreme polarization states  $\theta_m = 0, 90$  can be computed (see Sec. 2.2). Losses can be included in the computation of the scattering parameters. Input and output ports can be directly placed at the surface of the anisotropic material (i.e., liquid crystal in our case).

2. *Frequency-domain solver*: It can deal with non-diagonal permittivity/permeability tensors via the macro “Full Tensor Material”. Losses can be included in the computation. However, input and output ports cannot be directly placed at the surface of the anisotropic material. It means that isotropic layers have to be added to feed the structure, which requires a de-embedding process to characterize the structure under study. Fortunately, the software offers the possibility to change the reference planes of the input and output ports.

Both solvers were used in this work. As long as only extreme polarization states ( $\theta_m = 0, 90$ ) need to be simulated, it is preferable to use the time-domain solver because the de-embedding of the ports can be avoided. Frequency-domain solver offers a greater versatility since it allows to deal with non-diagonal tensors. However, a misapplication of the de-embedding process may cause additional error terms to the computation of the dispersion diagram. Length and relative permittivities of the de-embedding block should be carefully chosen in order to avoid unwanted resonances and minimize the error.

As a common feature of both time-domain and frequency-domain solvers, open boundary conditions, also known as Perfect Matching Layer (PML) in the literature, cannot touch the anisotropic material in *CST*. This issue can be solved by leaving an additional space (“Open Add Space” condition) between the structure and the open boundary condition.

As discussed throughout this work, the correct choice of the input/output modes in the unit cell of the periodic structure plays a fundamental role when applying the MMTMM. Many of the modes that are excited at the input/output ports do not have a physical correspondence with the modes that actually propagate in the unit cell. As the virtual waveguides associated with the input/output ports are conditioned by the boundary conditions that have to be imposed to these ports, the modes of these virtual waveguides are very often hardly related with the actual modes of the periodic structure. As an example, see that modes #2 and #3 in Fig. 10(a) are avoided for the computation of the dispersion diagram in this figure. In order to ensure a correct convergence of the method, these spurious (non-physical) modes should not be considered [24].

## References

- [1] M. Romagnoli *et al.*, “Graphene-based integrated photonics for next-generation datacom and telecom, *Nature Rev. Mater.*, vol. 3, pp. 392414, Oct. 2018.
- [2] Z. Gu *et al.*, “Resonant domain-wall-enhanced tunable microwave ferro-electrics, *Nature*, vol. 560, pp. 622627, Aug. 2018.
- [3] P. Yaghmaee, O. H. Karabey, B. Bates, C. Fumeaux, and R. Jakoby, “Electrically Tuned Microwave Devices Using Liquid Crystal Technology,” *Int. J. Antennas Propag.* vol. 2013, Article ID 824214, 2013.
- [4] J. Perruisseau-Carrier, “Graphene for antenna applications: Opportunities and challenges from microwaves to THz,” in *2012 Loughborough Antennas & Propagation Conference (LAPC)*, 2012.
- [5] J. B. L. Rao, D. P. Patel and V. Krichevsky, “Voltage-controlled ferroelectric lens phased arrays,” *IEEE Trans. Antennas Propag.*, vol. 47, no. 3, pp. 458-468, March 1999.
- [6] R. Reese *et al.*, “A Millimeter-Wave Beam-Steering Lens Antenna With Reconfigurable Aperture Using Liquid Crystal,” *IEEE Trans. Antennas Propag.*, vol. 67, no. 8, pp. 5313-5324, Aug. 2019.
- [7] O. Balci, N. Kakenov, and C. Kocabas, “Controlling phase of microwaves with active graphene surfaces,” *Appl. Phys. Lett.*, vol. 110, 161102, 2017.
- [8] Z. Zhao, X. Wang, K. Choi, C. Lugo and A. T. Hunt, “Ferroelectric Phase Shifters at 20 and 30 GHz,” *IEEE Trans. Microw. Theory Techn.*, vol. 55, no. 2, pp. 430-437, Feb. 2007.
- [9] R. Reese *et al.*, “Liquid Crystal Based Dielectric Waveguide Phase Shifters for Phased Arrays at W-Band,” *IEEE Access*, vol. 7, pp. 127032-127041, 2019.
- [10] M. Agiwal, A. Roy, and N. Saxena, “Next generation 5G wireless net- works: A comprehensive survey, *IEEE Commun. Surveys Tuts.*, vol. 18, no. 3, pp. 16171655, 2016.
- [11] N. W. Ashcroft and N. D. Mermin, *Solid State Physics*, Orlando: Harcourt, 1976.
- [12] R. E. Collin, *Field Theory of Guided Waves*, 2nd ed. New York: IEEE Press, 1990.
- [13] M. Tsuji, S. Matsumoto, H. Shigesawa, and K. Takiyama, “Guided-wave experiments with dielectric waveguides having finite periodic corrugation,” *IEEE Trans. Microw. Theory Techn.*, vol. 31, no. 4, pp.337344, 1983.
- [14] S. Amari, R. Vahldieck, J. Bornemann, and P. Leuchtmann, “Spectrum of corrugated and periodically loaded waveguides from classical matrix eigenvalues,” *IEEE Trans. Microw. Theory Techn.*, vol. 48, no. 3, pp.453460, 2000.
- [15] H. K. Liu and T. L. Dong, “Propagation characteristics for periodic waveguide based on generalized conservation of complex power technique,” *IEEE Trans. Microw. Theory Techn.*, vol. 54, no. 9, pp. 34793485, 2006.

- [16] F. Bongard, J. Perruisseau-Carrier, and J. R. Mosig, "Enhanced periodic structure analysis based on a multiconductor transmission line model and application to metamaterials," *IEEE Trans. Microw. Theory Techn.*, vol. 57, no. 11, pp. 2715-2726, 2009.
- [17] S. Marini, A. Coves, V. E. Boria, and B. Gimeno, "Efficient modal analysis of periodic structures loaded with arbitrarily shaped waveguides," *IEEE Trans. Microw. Theory Techn.*, vol. 58, no. 3, pp. 5295-536, 2010.
- [18] R. Islam, M. Zedler, and G. V. Eleftheriades, "Modal analysis and wave propagation in finite 2D transmission-line metamaterials," *IEEE Trans. Antennas Propag.*, vol. 59, no. 5, pp. 1562-1570, 2011.
- [19] A. Coves, S. Marini, B. Gimeno, and V. Boria, "Full-wave analysis of periodic dielectric frequency-selective surfaces under plane wave excitation," *IEEE Trans. Antennas Propag.*, vol. 60, no. 6, pp. 2760-2769, 2012.
- [20] Y. Weitsch and T. F. Eibert, "Modal series expansion of eigensolutions for closed and open periodic waveguides," *IEEE Trans. Antennas Propag.*, vol. 60, no. 12, pp. 5881-5889, 2012.
- [21] J. Naqui, A. Fernández-Prieto, M. Durn-Sindreu, F. Mesa, J. J. Martel, F. Medina, and F. Martn, "Common-mode suppression in microstrip differential lines by means of complementary split ring resonators: Theory and applications," *IEEE Trans. Microw. Theory Techn.*, vol. 60, no. 10, pp. 3023-3034, 2012.
- [22] F. Mesa, R. Rodríguez-Berral, and F. Medina, "On the computation of the dispersion diagram of symmetric one-dimensionally periodic structures, Symmetry (Basel), vol. 10, no. 8, p. 307, 2018.
- [23] M. Bagheriasl, O. Quevedo-Teruel, and G. Valerio, "Bloch analysis of artificial lines and surfaces exhibiting glide symmetry," *IEEE Trans. Microw. Theory Techn.*, vol. 67, no. 7, pp. 2618-2628, 2019.
- [24] F. Mesa, G. Valerio, R. Rodríguez-Berral, and O. Quevedo-Teruel, "Simulation-Assisted Efficient Computation of the Dispersion Diagram of Periodic Structures," *IEEE Antennas Propag. Mag.*, to be published.
- [25] H. Maune, M. Jost, R. Reese, E. Polat, M. Nickel, and R. Jakoby, "Microwave liquid crystal technology," *Crystals*, vol. 8, no. 9, p. 355, 2018.
- [26] P. G. de Gennes and J. Prost, *The Physics of Liquid Crystals*, 2nd ed. Oxford, U.K.: Clarendon, 1995.
- [27] J. Shekel, "Matrix Analysis of Multi-Terminal Transducers," *Proc. IRE*, vol. 42, no. 5, pp. 840-847, 1954.
- [28] T. Reveyrand, "Multiport conversions between S, Z, Y, h, ABCD, and T parameters, in 2018 Int. Work. Integr. Nonlinear Microw. Millimetre-wave Circuits, no. 6, 2018, pp. 13.
- [29] R. H. Chen, *Liquid Crystal Displays: Fundamental Physics and Technology*, Hoboken, NJ, USA: Wiley, 2011.
- [30] E. Polat *et al.*, "Tunable Liquid Crystal Filter in Nonradiative Dielectric Waveguide Technology at 60 GHz," *IEEE Microw. Wireless Compon. Lett.*, vol. 29, no. 1, pp. 44-46, Jan. 2019.
- [31] C. Ding, F. Meng, J. Han, H. Mu, Q. Fang and Q. Wu, "Design of Filtering Tunable Liquid Crystal Phase Shifter Based on Spoof Surface Plasmon Polaritons in PCB Technology," *IEEE Trans. Compon. Pack. Manuf. Technol.*, vol. 9, no. 12, pp. 2418-2426, Dec. 2019.
- [32] A. E. Prasetyadi *et al.*, "Continuously tunable substrate integrated waveguide bandpass filter in liquid crystal technology with magnetic biasing," *Electron. Lett.*, vol. 51, no. 20, pp. 1584-1585, 10 2015.
- [33] G. Perez-Palomino *et al.*, "Accurate and Efficient Modeling to Calculate the Voltage Dependence of Liquid Crystal-Based Reflectarray Cells," *IEEE Trans. Antennas Propag.*, vol. 62, no. 5, pp. 2659-2668, May 2014.
- [34] G. Perez-Palomino *et al.*, "Design and Demonstration of an Electronically Scanned Reflectarray Antenna at 100 GHz Using Multiresonant Cells Based on Liquid Crystals," *IEEE Trans. Antennas Propag.*, vol. 63, no. 8, pp. 3722-3727, Aug. 2015.
- [35] W. Fuscaldo *et al.*, "Tunable FabryPerot Cavity THz Antenna Based on Leaky-Wave Propagation in Nematic Liquid Crystals," *IEEE Antennas Wireless Propag. Lett.*, vol. 16, pp. 2046-2049, 2017.
- [36] M. Nickel *et al.*, "Ridge Gap Waveguide Based Liquid Crystal Phase Shifter," *IEEE Access*, vol. 8, pp. 77833-77842, 2020.
- [37] M. Jost *et al.*, "Miniaturized Liquid Crystal Slow Wave Phase Shifter Based on Nanowire Filled Membranes," *IEEE Microw. Wirel. Compon. Lett.*, vol. 28, no. 8, pp. 681-683, Aug. 2018.
- [38] H. Gruler, T. J. Scheffer, and G. Meier, "Elastic Constants of Nematic Liquid Crystals, *Zeitschrift fr Naturforschung A*, vol. 27, no. 6, pp. 966-976, 1972.
- [39] A. Alex-Amor *et al.*, "Analytical approach of director tilting in nematic liquid crystals for electronically tunable devices," *IEEE Access*, vol. 7, pp. 148831-14893, 2019.
- [40] A. Alex-Amor, . Palomares-Caballero, A. Palomares, A. Tamayo-Domnguez, J. M. Fernndez-Gonzlez, and P. Padilla, "Generalized director approach for liquid-crystal-based reconfigurable RF devices," *IEEE Microw. Wireless Compon. Lett.*, vol. 29, no. 10, Oct. 2019.
- [41] A. D. Berk, "Variational principles for electromagnetic resonators and waveguides," *IRE Trans. Antennas Propag.*, no. 4, pp. 1041-111, 1956.
- [42] J. B. Davies, "Propagation in rectangular waveguide filled with skew uniaxial," *IEEE Trans. Microw. Theory Techn.*, vol. 15, no. 6, pp. 372-376, 1967.
- [43] K. Sun, J. K. Lee, and J. W. Graham, "Fields and wave modes analysis of rectangular waveguide filled with uniaxial medium," *IEEE Trans. Microw. Theory Techn.*, vol. 64, no. 11, pp. 3429-3440, 2016.
- [44] R. James, F. A. Fernandez, S. E. Day, S. Bulja and D. Mirshekar-Syahkal, "Accurate Modeling for Wideband Characterization of Nematic Liquid Crystals for Microwave Applications," *IEEE Trans. Microw. Theory Techn.*, vol. 57, no. 12, pp. 3293-3297, Dec. 2009.
- [45] R. James, F. Anibal Fernandez, S. E. Day, S. Bulja, D. Mirshekar-Syahkal and M. Yazdanpanahi, "Finite element analysis of a balanced microstrip line filled with nematic liquid crystal," *2009 IEEE MTT-S International Microwave Symposium Digest*, Boston, MA, 2009, pp. 133-136.
- [46] P.-S. Kildal, A. U. Zaman, E. Rajo-Iglesias, E. Alfonso and A. Valero-Nogueira, "Design and experimental verification of ridge gap waveguide in bed of nails for parallel-plate mode suppression," *IET Microw. Antennas Propag.*, vol. 5, no. 3, pp. 262-270, Feb. 2011.
- [47] S. Ma *et al.*, "Liquid Crystal Leaky-Wave Antennas With Dispersion Sensitivity Enhancement," *IEEE Trans. Compon. Pack. Manuf. Technol.*, vol. 7, no. 5, pp. 792-801, May 2017.
- [48] S. Paulotto, P. Baccarelli, F. Frezza, and D. R. Jackson, "A novel technique for open-stopband suppression in 1-D periodic printed leaky-wave antennas," *IEEE Trans. Antennas Propag.*, vol. 57, no. 7, pp. 1894-1906, 2009.
- [49] J. T. Williams, P. Baccarelli, S. Paulotto, and D. R. Jackson, "1-D combline leaky-wave antenna with the open-stopband suppressed: Design considerations and comparisons with measurements," *IEEE Trans. Antennas Propag.*, vol. 61, no. 9, 2013.